This is the peer-reviewed, final accepted version for American Mineralogist, published by the Mineralogical Society of America.
The published version is subject to change. Cite as Authors (Year) Title. American Mineralogist, in press.
DOI: https://doi.org/10.2138/am-2022-8257. http://www.minsocam.org/

Revision 1

The influence of Al_2O_3 on the structural properties of $MgSiO_3$ akimotoite

Nicki C. Siersch[1,*], Giacomo Criniti[1], Alexander Kurnosov[1], Tiziana Boffa Ballaran[1], Zhaodong Liu[1,2], Takayuki Ishii[1,**], Daniel J. Frost[1], Tony Yu[3], Yanbin Wang[3]

[1] Bayerisches Geoinstitut, Universität Bayreuth, D-95440 Bayreuth, Germany.

[2] State Key Lab of Superhard Materials, Jilin University, CHN-130000 Changchun, China.

[3] Center for Advanced Radiation Sources, The University of Chicago, Chicago, IL 60637, USA.

[*] Corresponding author: nicki.siersch@upmc.fr; present address: Sorbonne Université, Muséum National d'Histoire Naturelle, UMR CNRS 7590, Institut de Minéralogie, de Physique des Matériaux et de Cosmochimie, IMPMC, Paris, France.

[**] present address: Center for High Pressure Science and Technology Advanced Research, CHN-100094, Beijing, China.

nicki.siersch@upmc.fr

giacomo.criniti@uni-bayreuth.de

alexander.kurnosov@uni-bayreuth.de

tiziana.boffa-ballaran@uni-bayreuth.de

liu_zhaodong@jlu.edu.cn

takayuki.ishii@hpstar.ac.cn

dan.frost@uni-bayreuth.de

tyu@cars.uchicago.edu

wang@cars.uchicago.edu

Abstract

Akimotoite, a $MgSiO_3$ polymorph, present in the lower transition zone within ultramafic portions of subducting slabs and potentially also in the ambient mantle, will partition some amount of Al, raising the question of how this will affect its crystal structure and properties. In this study, a series of samples along the $MgSiO_3$ akimotoite - Al_2O_3 corundum solid solution have been investigated by means of single-crystal X-ray diffraction in order to examine their crystal chemistry. Results show a strong non-linear behavior of the *a*- and *c*-axes as a function of Al content, which arises from fundamentally different accommodation mechanisms in the akimotoite and corundum structures. Furthermore, two Al_2O_3-bearing akimotoite samples were investigated at high pressure in order to determine the different compression mechanisms associated with Al substitution. Al_2O_3-bearing akimotoite becomes more compressible at least up to a content of 20 mol% Al_2O_3, due likely to an increase in compressibility as the Al cation is incorporated into the SiO_6 octahedron. This observation is in strong contrast to the stiffer corundum end-member having a K_T = 250 GPa larger than that of the akimotoite end-member (K_T = 205(1) GPa). These findings have implications for mineral physics models of elastic properties, which have in the past assumed linear mixing behavior between the $MgSiO_3$ akimotoite and Al_2O_3 corundum end-members in order to calculate sound wave velocities for Al-bearing akimotoite at high pressure and temperature.

Keywords: akimotoite, corundum, X-ray diffraction, high-pressure, solid solution

Introduction

Akimotoite is an $MgSiO_3$ polymorph, with an ilmenite-type structure (Kawai et al. 1974; Horiuchi et al. 1982), that is stable between 20 and 24 GPa and 1373 to 1973 K (Ito and Yamada

1982; Sawamoto 1987; Gasparik 1990). This polymorph crystallizes in the $R\bar{3}$ space group with a distorted hexagonal close packed setting of oxygen atoms and cations occupying octahedral interstitial sites (Figure S1a). The MgO_6 and SiO_6 octahedra form distinct layers of face-sharing octahedra; with the MgO_6 octahedra being much more distorted than the SiO_6 octahedra (Horiuchi et al. 1982) due to a larger shift of the Mg^{2+} cation from the center of the octahedron. In an ideal ilmenite-type structure, Mg and Si are completely ordered in alternating layers along the *c*-axis. Although the stability field of this mineral was determined to be rather small (e.g. Ito and Yamada 1982; Sawamoto 1987; Gasparik 1990), its possible presence near the base of the Earth's transition zone (e.g. Ishii et al. 2011; Kato et al. 2014; Ishii et al. 2019a) might explain the relatively high seismic velocities and observations of seismic anisotropy at this depth (e.g. Wookey et al. 2002; Vavryčuk 2006; Irifune et al. 2008; Shiraishi et al. 2008; Foley and Long 2011; Zhou et al. 2014; Nowacki et al. 2015; Pamato et al. 2016; Siersch et al. 2021).

The $MgSiO_3$ ilmenite-type structure was named akimotoite after its discovery in the Tenham L6 chondritic meteorite, which mainly consists of olivine and hypersthene and a network of <1 mm thin shock-induced veins (Sharp et al. 1997; Tomioka and Fujino 1997; Miyajima et al. 2007). In these veins, akimotoite coexists with bridgmanite, majorite and ringwoodite having a maximum grain size of ~0.3 to 3 μm in length (Sharp et al. 1997; Tomioka and Fujino 1997; Miyajima et al. 2007). Analyses of the composition of the crystallized akimotoite grains revealed chemical variations of up to 13.54 wt% FeO, 10.46 wt% Al_2O_3, 0.69 wt% Cr_2O_3, and 0.38 wt% CaO (Sharp et al. 1997; Tomioka and Fujino 1997; Miyajima et al. 2007). Experimental studies have shown that the Al incorporation follows a coupled substitution mechanism: $Mg^{2+} + Si^{4+} = 2\ Al^{3+}$ and extends up to the pyrope composition $Mg_3Al_2Si_3O_{12}$ (25 mol% Al_2O_3) between 25 and 27 GPa at temperatures below 1500 K (Irifune and Ringwood 1987; Kubo and Akaogi 2000; Akaogi et al. 2002). The Al_2O_3 end-member in the akimotoite binary solid solution is often assumed to be Al_2O_3 corundum (e.g. Stixrude and Lithgow-

Bertelloni 2011), which is structurally similar to $MgSiO_3$ akimotoite, having the $R\bar{3}c$ space group. As in the akimotoite structure, layers of AlO_6 face-sharing octahedra lie along the *c*-axis but the increase in symmetry is due to the fact that all the cation sites in the structure are equivalent (Figure S1b). Previous studies (Liu 1977; Kanzaki 1987; Akaogi et al. 2002) have investigated the $MgSiO_3$ - Al_2O_3 akimotoite solid solution by means of powder X-ray diffraction up to 25 mol% Al_2O_3 and reported a strong non-linear evolution of the unit-cell parameters *a* and *c* as a function of Al_2O_3 content. Aside from corundum itself there is little structural information on the Al_2O_3-rich side of the apparent compositional gap, although phase equilibria studies show that up to 37 mol% $MgSiO_3$ can substitute into corundum with increasing temperature (Liu et al. 2016; 2017). Besides the $MgSiO_3$ akimotoite and Al_2O_3 corundum end-members, no structural refinements on Al_2O_3-bearing akimotoite or $MgSiO_3$-bearing corundum have been performed to date. This, however, is important for understanding how samples with mixed compositions accommodate cations with such different sizes, determining whether there could be a complete solid solution between these two end-members and whether elastic properties of the end-members are suitable for describing properties of the solid solution.

Akimotoite was found in several experimental studies to have a strong axial anisotropy with the *c*-axis being much more compressible relative to the stiffer *a*-axis (Reynard et al. 1996; Wang et al. 2004; Siersch et al. 2021). On the other hand, the axial compressibility of the Al_2O_3 corundum end-member appears to be isotropic (d'Amour et al. 1978; Finger and Hazen 1978). Neither the structural mechanism from which the axial anisotropy stems from, nor why it is affected by Al incorporation are understood.

The objectives of this study are two-fold: first to synthesize single-crystals along the $MgSiO_3$ akimotoite-Al_2O_3 corundum join in order to elucidate the mixing behavior of this solid solution and to constrain the crystal chemistry of mixed compositions by means of single-crystal X-ray

diffraction and second, to investigate the high-pressure behavior of samples belonging to the akimotoite-corundum solid solution in order to determine the different compression mechanisms associated with this substitution.

Methods

Sample synthesis

The synthesis of large single-crystals of the $MgSiO_3$ akimotoite end-member is described in detail by Siersch et al. (2021). Single-crystals for all other compositions have been synthesized from stoichiometric mixtures of MgO, SiO_2, Al_2O_3 and/or $Al(OH)_3$ oxides ground in an agate mortar under ethanol for one hour to produce fine-grained homogenous powders. $Al(OH)_3$ or $MgCl_2$ were added as a flux during the syntheses to enhance crystal growth (Table 1). Two additional starting glasses with nominal compositions $Mg_{0.975}Al_{0.050}Si_{0.975}O_3$ (Ak98) and $Mg_{0.8}Al_{0.4}Si_{0.8}O_3$ (Ak80), were produced from mixtures of MgO, SiO_2 and Al_2O_3 oxides, finely ground in ethanol in an agate mortar for one hour. These mixtures were then heated up to 1873 K in a furnace for 4 hours and then quenched in an icy water bath to produce glasses. The glasses were subsequently ground in order to obtain fine-grained homogeneous starting materials.

Synthesis experiments were performed either in the Sumitomo 1200 tonne multi-anvil press with a split sphere-type guide block (Keppler and Frost 2005) or Iris 1500 tonne multi-anvil press with the Osugi-type guide block (Ishii et al. 2016; 2019b) at the Bayerisches Geoinstitut, University of Bayreuth, Bayreuth (BGI). For the single-crystal syntheses, the starting materials were packed into Pt capsules, which were then carefully closed with a Lampert PUK U3 welder operating in micro mode (power: 7 %, time: 3-5 ms) to ensure that water could not escape. 10/4 assemblies were used with $LaCrO_3$ furnaces at pressures of 22 and 24 GPa in the Sumitomo

press. The assemblies comprised a 10 mm edge length Cr_2O_3-doped MgO octahedron and were used with F08 grade WC anvils with 4 mm truncation edge lengths (TEL). The temperature was monitored using a D-type thermocouple ($W_{97}Re_3$-$W_{75}Re_{25}$) that was inserted from the top and positioned as close to the capsule as possible. To generate pressures of ~27 GPa, experiments in the Iris-1500 tonne press were performed with standard 7/3 assemblies, with a 7 mm octahedron equipped with a $LaCrO_3$ furnace and 3 mm TEL TF05 grade WC anvils.

For the synthesis of polycrystalline samples, a modified 7/3 assembly was used. The starting materials were placed into Mo-foil capsules that also acted as furnaces and were then inserted into a ZrO_2 sleeve and a Cr_2O_3-doped MgO octahedron. Connection between the furnace and the anvils was ensured by 0.5 mm thick Mo wires that were placed inside two ZrO_2 spacers positioned at the top and bottom of the Mo capsule. The temperature was monitored using a D-type thermocouple ($W_{97}Re_3$-$W_{75}Re_{25}$) that was inserted through pre-drilled holes at the center of the octahedron. Synthesis details are reported in Table 1.

Sample characterization

Both polycrystalline and single-crystal recovered samples were polished in epoxy holders for scanning electron microscopy (SEM) and electron microprobe (EMP) analyses. A LEO 1530 scanning electron microscope was employed to obtain an overview of the crystallized run products and their size distribution, whereas a JEOL JXA-8200 EMP was used for quantitative chemical analyses of the different samples. The electron microprobe was calibrated using standards of enstatite, for Mg and Si, spinel, for Al, and Pt-metal. A minimum of 20 points were measured on each sample. During the measurements the voltage and current were set to 15 kV and 15 nA, respectively, and a focused beam was used. The resulting averaged compositions and sizes of the recovered akimotoite and corundum crystals are reported in Table 1. The water content in the $MgSiO_3$ akimotoite end-member was determined by means of Fourier-transform

infrared (FTIR) spectroscopy (Siersch et al. 2021) and was found to be relatively minor (281 ppm wt H_2O), in agreement with previous studies on water incorporation into akimotoite (e.g. Bolfan-Casanova et al. 2000). Similar minor water contents are expected for the other single-crystals in the solid solution synthesized in a hydrous environment (Ak99, Cor92, Cor97 and Cor100, Table 1) following present literature data on H_2O contents in akimotoite and corundum (e.g. Bolfan-Casanova et al. 2000; Beran and Rossman 2006; Siersch et al. 2021). However, due to the small crystal sizes and the presence of fluid inclusions in the corundum-rich samples, it was not possible to perform FTIR measurements. As shown in the results section, however, the lack of scatter in the structural data suggests that our hypothesis of low water contents is likely correct.

Room pressure and high-pressure single crystal X-ray diffraction and structural refinements

High quality single-crystals from each run-product were selected based on their sharp reflection profiles in omega scans, with full-width at half maximum between 0.05° and 0.09°. A Huber four-circle diffractometer with a Eulerian cradle geometry equipped with a point detector and a Mo$K\alpha$ (λ = 0.71073 Å) source operated at 50 kV and 40 mA was used. Eight-position centering of up to 28 reflections for each sample was performed to determine accurate unit-cell lattice parameters at ambient conditions (Table 2).

Full intensity data collections for structural refinements at ambient conditions were performed on an Oxford Diffraction Xcalibur diffractometer equipped with a graphite monochromator, Mo$K\alpha$ radiation operated at 50 kV and 40 mA and a Sapphire 2 CCD detector. Complete and redundant intensity data were collected using ω scans with a width of 1° and a default time of 5 to 10 s in a 2θ range between 2 and 75°. Intensity data collection on one small crystal of

sample S7179 (less than 30 μm in size) was performed on a Bruker IμS Inside diffractometer using Ag$K\alpha$ radiation (λ = 0.55941 Å) operated at 50 kV and 880 μA, with a beam size of 50 μm. The crystal was measured in a 2θ range between 4 and 29° using an exposure time of 40 s. The intensity data were integrated using the CrysAlis 171.36.28 software. Lorentz and polarization corrections, as well as an empirical absorption correction, were performed.

One high-quality single-crystal of $MgSiO_3$ akimotoite, Ak100, with sharp omega reflection profiles that had full-widths at half maxima of 0.08°, was chosen for the collection of full intensity data at high pressure. The crystal was polished to 15 μm thickness having the final dimensions of 100x100x15 μm^3. One BX90 type diamond anvil cell (DAC) was prepared with diamond culets of 400 μm diameter, glued into Boehler-Almax seats with an opening angle of 90° (Kantor et al. 2012). A Re gasket with an original thickness of 200 μm was pre-indented to a thickness of 61(1) μm. A hole with a diameter of 230 μm was laser-cut into the center of this indentation to produce the sample chamber. The single-crystal was loaded inside the DAC together with a small ruby sphere of 10 μm diameter placed next to the crystal for pressure determination. The DAC was gas loaded with neon gas as a pressure transmitting medium using the gas-loading system installed at the BGI (Kurnosov et al. 2008). After each pressure increase, the DAC was left to stabilize for at least one day to avoid any pressure changes during the XRD measurements. The ruby fluorescence was measured before and after each XRD measurement using a Horiba LABRAM HR Raman micro-spectrometer equipped with an 1800 g/mm grating and a He-Ne-laser (λ = 632.8 nm) with 20 mW laser power. Pressures were determined according to the calibration reported by Dewaele et al. (2004). Eight-position centering of up to 17 reflections at each pressure point was performed to determine accurate unit-cell lattice parameters of the $MgSiO_3$ akimotoite single-crystal (Table 3) using a Huber four-circle diffractometer. Full intensity data were collected at 4 pressure points using the Oxford Diffraction Xcalibur diffractometer described above. For measurements performed on the

crystal in the DAC, ω scans with a width of 1° and a default time of 60 s in a 2θ range between 2 and 70° were employed. In addition, the cell was not tilted or reversed during the data collection. Additional to the Lorentz and polarization corrections, an analytical absorption correction was taken into account due to the partial absorption of the incident and diffracted X-ray beams by the diamond anvils, the Re gasket, the pressure transmitting medium and the crystal itself, by using the numerical absorption correction Absorb6.0, written by Angel (2004) and implemented into the CrysAlis absorption correction software.

The integrated intensity data, collected both at room conditions and at high pressures, were used for structural refinements in the ShelX software (Sheldrick 2008) integrated in the WinGX program system (Farrugia 1999). For measurements at ambient conditions, neutral scattering factors for Mg, Al, Si and O were used. The occupancies of Mg, Al and Si at the octahedral site of the $R\bar{3}c$ structure (corundum-type structure) were fixed to the values obtained from the microprobe analyses due to their similar electron density. A careful analysis of all $MgSiO_3$-rich corundum single-crystals indicated no evidence for cation ordering except for Cor81, which revealed the presence of the *003* reflection, that is normally extinct in space group $R\bar{3}$c, albeit with very low intensity. This suggests an incipient ordering of Mg and Si into the corundum structure. No other reflections consistent with space group $R\bar{3}$ were detected and the Cor81 sample was, therefore, refined in the $R\bar{3}$c space group. For Ak100 and Ak99, Mg and Si were considered perfectly ordered in the two distinct octahedral sites of the $R\bar{3}$ structure (akimotoite-type structure) and the small amount of Al of the Ak99 sample was equally distributed between the two octahedral sites assuming the coupled substitution $Mg^{2+} + Si^{4+} = 2\ Al^{3+}$, as also suggested for Cr-bearing akimotoites (Bindi et al. 2014). All cations and oxygen sites were refined anisotropically. Between 136 and 378 unique reflections were used to refine 10 (for corundum-type structures, Figure S1b) to 16 (for akimotoite-type structures, Figure S1a) parameters.

For the high-pressure study, structural refinements of $MgSiO_3$ akimotoite up to 10.83(3) GPa (space group $R\bar{3}$) were performed by using neutral scattering factors for Mg, Si and O, assuming perfect ordering of Mg and Si into the two distinct octahedra. The cations were refined anisotropically whereas the oxygen was refined isotropically in order to decrease the number of refined parameters, since the number of collected reflections is reduced due to obstruction from the DAC. Between 147 to 151 reflections were used to refine 11 parameters at each pressure point.

Refinement details, anisotropic and isotropic displacement parameters, atomic coordinates and bond distances for all samples investigated in this study, both at room and at high pressure, can be found in the deposited Crystallographic Information File (CIF).

Powder X-ray diffraction at high-pressure

High-pressure X-ray diffraction in combination with ultrasonic experiments were performed in the 1000 tonne large volume press at the 13-ID-D beamline of GSECARS at the APS. A 10/4 multi-anvil assembly was modified to fit a cylindrical rhenium (Re) furnace prepared from 25 μm thick Re foil. Two windows were laser cut into the furnace wall and aligned to the X-ray beam path to allow the incident and diffracted X-ray beams to pass through the sample without interference from the Re. Powder X-ray diffraction patterns were collected at high pressure using an energy-dispersive system at a fixed 2θ angle of 6.04° operating between 42 and 112 keV. The unit-cell parameters of the two polycrystalline samples, Ak98 and Ak80, were determined using full profile LeBail refinements with the GSAS software package in the EXPGUI interface (Toby 2001, Larson and Von Dreele 2004) and are reported in Table 3. Pressures were obtained from the simultaneous measurements of X-ray diffraction and acoustic wave velocities (Siersch 2019). Only room temperature high-pressure X-ray diffraction results

on the akimotoite samples are reported here. The results of the ultrasonic measurements will be reported elsewhere.

Results and Discussion

$MgSiO_3$ – Al_2O_3 solid solution behavior

The unit-cell volumes measured at ambient conditions of the eight single-crystals and two polycrystalline samples belonging to the akimotoite - corundum solid solution (Table 2 and Table 3) are plotted in Figure 1a as a function of Al_2O_3 content. Literature data (Liu 1977; Kanzaki 1987; Irifune et al. 1996; Akaogi et al. 2002; Wang et al. 2004; Liu et al. 2016; 2017; Higo et al. 2018) for the same solid solution are reported for comparison. The unit-cell volumes of $MgSiO_3$ akimotoite (Wang et al. 2004) and of Al_2O_3 corundum (Higo et al. 2018) show larger values than those obtained from our single-crystal study, which most likely results from the use of less accurate energy-dispersive X-ray diffraction measurements performed on polycrystalline samples. The corundum end-member volume reported by Liu (1977) and the akimotoite end-member volumes of previous studies (Kanzaki 1987; Akaogi et al. 2002) on the other hand are in perfect agreement with the data obtained in this study. The majority of the data follow the linear dashed line joining the two end-member values obtained in this study (Figure 1a). The variations of the *a*- and *c*-axes with Al_2O_3 content, on the other hand, are strongly non-linear (Figures 1b, c). The *a* lattice parameter (Figure 1b) increases rapidly with increasing Al_2O_3 component in the akimotoite structure or when $MgSiO_3$ is incorporated into the corundum structure. On the other hand, the *c* lattice parameter (Figure 1c) has a negative deviation from linearity at both ends of the solid solution. These opposite behaviors give rise to the practically linear behavior of the unit-cell volume variation along the $MgSiO_3$ akimotoite-Al_2O_3 corundum join, observed in Figure 1a. The behavior of the unit-cell axes at the two ends of the akimotoite-corundum solid solution do not seem to display typical excess property

behavior, as the corundum side, in particular, appears too linear to be part of a single curve for the entire solution.

The effect of Al_2O_3 substitution on the unit-cell lattice parameter of akimotoite can be compared to that arising from Cr_2O_3 substitution. Both corundum and eskolaite, Cr_2O_3, crystallize in the $R\bar{3}c$ structure and Cr^{3+} has a slightly larger size (0.615 Å) than Al^{3+} (0.535 Å) (Shannon 1976). The lattice parameters of these two compounds, however, are very different, with Cr_2O_3 having a much larger unit-cell than akimotoite (Ovsyannikov and Dubrovinsky 2011) resulting in a unit-cell volume 31.2 $Å^3$ larger than that of Al_2O_3 (out of scale in Figure 1a). The larger unit-cell lattice parameters of the eskolaite structure with respect to both corundum and akimotoite may be due to the fact that this compound is antiferromagnetic at room conditions (McGuire et al. 1956). The change in unit-cell parameters *a*, *c* and *V* of akimotoite as a function of Cr_2O_3 content (Bindi et al. 2014) are plotted in Figures 1a-c and indicate a linear mixing relationship along the $MgSiO_3$ - Cr_2O_3 join, in contrast to the non-linearity observed for the unit-cell axes along $MgSiO_3$-Al_2O_3 join. It is difficult to understand why these two solid solutions behave so differently, which is further hindered by the fact that at present there are no studies that have looked at the incorporation of Mg and Si into the eskolaite structure.

Structural refinements on eight single-crystals along the $MgSiO_3$-Al_2O_3 solid solution were performed in order to determine the structural mixing behavior. Figure 2 shows the variation of the octahedral volumes of the MgO_6 and SiO_6 octahedra and the AlO_6/CrO_6 octahedra along the $MgSiO_3$-Al_2O_3/Cr_2O_3 solid solutions. The average of MgO_6 and SiO_6 octahedral volumes in akimotoite are also shown for better comparison with the AlO_6 and CrO_6 octahedral volumes. As the Al or Cr contents increase in the akimotoite structure, the MgO_6 octahedral volume decreases as expected given the substitution of a smaller cation at that site, whereas the SiO_6 volume increases due to the incorporation of a larger cation. These changes are more pronounced along the Cr substitution. Interestingly on the corundum-rich end, only a small

change can be observed in the AlO_6 octahedral volumes as the concentration of $MgSiO_3$ increases. This is surprising since the opposite effect of Al_2O_3 incorporation in akimotoite appears to be very pronounced. The difference may be due to the fact that whilst two Al are substituting a Mg and Si occupying two adjacent layers in the akimotoite structure, preserving in this way cation ordering to a certain extent, (Figure S1a), Mg and Si may substitute two Al in any octahedral site (Figure S1b) maintaining a random distribution and a $R\bar{3}c$ symmetry even up to a 25 mol% $MgSiO_3$ content.

The linear behavior between the octahedral volumes of corundum and eskolaite and the average octahedral volumes of the Al_2O_3/Cr_2O_3-bearing akimotoites respectively (Figure 2), which can be considered to describe a hypothetical $R\bar{3}c$ disordered solid solution, mimic the unit-cell volume changes along the two solid solutions (Figure 1a). Assuming a linear change also for the volumes of the MgO_6 and SiO_6 octahedra as a function of Al_2O_3/Cr_2O_3 content, two significantly different behaviors are observed (Figure 2). The two linear trends describing the behavior of the Cr-bearing akimotoites cross the linear trend describing the $R\bar{3}c$ hypothetical $MgSiO_3$-Cr_2O_3 solid solution at ~ 0.3 Cr_2O_3 mol, suggesting that samples having compositions above ~ 0.3 mol of Cr_2O_3 may already have complete cation disorder and have the $R\bar{3}c$ space group. Octahedral volumes for the Ak100 and Ak99 single crystals, on the other hand, suggest that linear trends describing the Al-akimotoites reach the $R\bar{3}c$ hypothetical $MgSiO_3$-Al_2O_3 join practically at the Al_2O_3 end-member, suggesting that the $R\bar{3}$ and $R\bar{3}c$ $MgSiO_3$-Al_2O_3 systems are two distinct solid solutions. Substitution of Al_2O_3 into akimotoite has a much larger effect on its structure than $MgSiO_3$ substitution into corundum, whose structure is able to accommodate quite a large amount of Mg and Si without major changes in the octahedral volume and distortion, as can be seen in the change of the octahedral angle variance (OAV) reported in the supplementary material (Figure S2). This suggests that an immiscibility gap may be present around the 50:50 compositions in this solid solution, in stark contrast to the linear

behavior observed for the $MgSiO_3$-Cr_2O_3 solid solution which may well turn out to be a complete solid solution.

Two further structural features may help to explain the contrasting behavior of the unit-cell axes in the akimotoite-corundum systems. The change with Al_2O_3 content of the distance between the two oxygens along the edges of the shared faces of MgO_6 and SiO_6 octahedra (Figure S1a) for akimotoite and AlO_6 octahedra for corundum (Figure S1b) in the (110) plane (Figure 3) increases rapidly on both the akimotoite as well as the corundum-rich sides. By connecting the two end-members, a positive non-linear behavior can be clearly identified (Figure 3). This behavior is likely responsible for the non-linear evolution of the *a* unit-cell lattice parameter (Figure 1b). In fact, a linear increase of the same O···O distance is observed along the $MgSiO_3$-Cr_2O_3 system directly comparable to the linear increase of the *a*-axis in this solid solution. On the other hand, the distance between the oxygens that describe the height of the two face-sharing octahedral layers along the *c*-axis, follows a negative non-linear behavior (Figure 4) which is clearly responsible for the evolution of the *c*-axis (Figure 1c). For the $MgSiO_3$-Cr_2O_3 solid solution, however, this trend is again linear as indicated by the dashed line in Figure 4.

High-pressure structural evolution of $MgSiO_3$ akimotoite

The variation of the unit-cell lattice parameters with pressure (Table 3) of a single-crystal of $MgSiO_3$ akimotoite measured in the DAC as part of this study (Figures 5a and b) is in excellent agreement with that reported by Siersch et al. (2021). The eight unit-cell data points collected in this study are satisfactorily described by the third-order Birch-Murnaghan EoS (BM3 EoS) that were fitted using the program EoSFit7GUI (Angel et al. 2014; Gonzalez-Platas et al. 2016) with isothermal bulk modulus K_{T0} = 205(1) GPa and first pressure derivative K_0' = 4.9(2) and by the two linearized BM3 EoS with M_{a0} = 728(6) GPa, M_{a0}' = 16.0(7) and M_{c0} = 470(2) GPa,

342 M_{c0}' = 12.6(3) reported in Siersch et al. (2021) (solid black lines in Figures 5a and b). As shown
343 by the two multi-anvil experiments performed on polycrystalline samples, with increasing Al
344 content, akimotoite becomes more compressible (Figure 5a) with isothermal bulk moduli of K_{T0}
345 = 204(1) GPa and K_0' = 4.9(1) for Ak98 and K_{T0} = 198(1) GPa and K_0' = 5.2(1) for Ak80. This
346 is in contrast to the very stiff corundum end-member (d'Amour et al. 1978, Figure 5a), which
347 has a K_{T0} = 251(35) GPa with K_0' fixed to the value of 4 (2nd order Birch-Murnaghan EoS,
348 BM2). The uncertainty of K_{T0} obtained from this fit is very large but the bulk modulus is in
349 agreement with other K_{T0} reported in literature of 250(2) GPa (Higo et al. 2018) and 254(8)
350 GPa (Dewaele and Torrent 2013). The non-linear behavior of the bulk modulus along the
351 akimotoite-corundum solid solution is a striking feature of this system and also suggests a
352 different structural response of the two end-members when accommodating cation substitution.

353 Although the excess molar volume (V^{ex}) along the akimotoite-corundum join is small at room
354 pressure (Figure 1a), because Al_2O_3 reduces the bulk modulus of akimotoite in comparison to
355 both end members there is the potential for an increase in V^{ex} with pressure. Using the
356 compressibility of the Ak80 sample, an estimate for the symmetric V^{ex} can be made at pressure
357 and fitted using a Margules parameter (W_V), i.e.:

358 $$V^{ex} = W_V * X * (1 - X)$$

359 where X is the mole fraction of Al_2O_3 in Akimotoite. This is a minimum estimate as the data
360 only extend to 20 % Al_2O_3, however, a W_V of -0.354 cm^3/mol is determined at 10 GPa and -
361 0.52 cm^3/mol at 20 GPa, with the resulting curves for V^{ex} at high pressure plotted in Figure
362 S3. These excess parameters are significant and should probably be considered when
363 performing thermodynamic calculations for the Al content of akimotoite.

364 The Al substitution also has a major effect on the compressibility of the unit-cell axes (Figure
365 5b). The *a*-axis becomes more compressible with increasing Al content, whereas the *c*-axis

366 becomes less compressible resulting in a decrease of the large axial anisotropy of $MgSiO_3$
367 akimotoite. Linearized BM3 EoS have been used to fit the *P* versus unit-cell axis data, resulting
368 in M_{a0} = 758(12) GPa, M_{a0}' = 9(1) and M_{c0} = 451(21) GPa, M_{c0}' = 19(3) for Ak98 and M_{a0} =
369 610(27) GPa, M_{a0}' = 18(3) and M_{c0} = 593(45) GPa, M_{c0}' = 8(4) for Ak80. Note that the unit-
370 cell parameters reported by d'Amour et al. (1978) show a nearly isotropic compressibility for
371 corundum within the uncertainties, resulting in the EoS parameters M_{a0} = 788(109) GPa and
372 M_{c0} = 685(96) GPa, with M_0' fixed to the value of 12. Both axial incompressibilities, and in
373 particular that of the *c*-axis, are larger than those obtained for akimotoite, explaining the larger
374 bulk modulus of Al_2O_3. The variation of the *c/a* ratio with pressure (Figure 5c) reflects the
375 decrease in anisotropy of the axial compressibility with increasing Al content. While the Ak100
376 and Ak98 samples show a strong decrease of the *c/a* with pressure, such a decrease is only
377 slightly visible for sample Ak80 and corundum shows an isotropic axial compressibility at least
378 up to 10 GPa (d'Amour et al. 1978). Note, however that for Ak98 the variation of the *c/a* ratio
379 is similar to that of the end-member only at low pressure, at pressures larger than 17 GPa it
380 remains almost constant suggesting a change in compression behavior.

381 In order to understand the change in axial compressibility with increasing Al content, structural
382 refinements on $MgSiO_3$ akimotoite were performed using intensity data collected at four
383 pressure points and compared to the Al_2O_3 corundum end-member (d'Amour et al. 1978). The
384 MgO_6 and SiO_6 octahedral volumes of $MgSiO_3$ akimotoite decrease smoothly with increasing
385 pressure and were fitted with linear BM2 EoS (Figure 6). The MgO_6 octahedra are significantly
386 more compressible than the SiO_6 octahedra (K_0 = 149(2) GPa and K_0 = 327(32) GPa,
387 respectively) in good agreement with data reported by Yamanaka et al. (2005). The AlO_6
388 octahedral volume of the corundum end-member (d'Amour et al. 1978) also decrease smoothly
389 having an intermediate incompressibility of K_0 = 251(35) GPa compared to the MgO_6 and SiO_6
390 octahedra. Note that the average incompressibility of the MgO_6 and SiO_6 octahedra is slightly

smaller (238 GPa) than the incompressibility of corundum, reflecting the fact that Al_2O_3 is stiffer than $MgSiO_3$ akimotoite. It appears that softening of the SiO_6 octahedra due to substitution of Al plays a more important role on the compressibility of Al-bearing akimotoites than the stiffening of the MgO_6 octahedra due to the same substitution, resulting in Al-bearing akimotoites being more compressible than the $MgSiO_3$ end-member.

The axial compressibility of akimotoite is highly anisotropic with the *c*-axis much more compressible than the *a*-axis (Reynard et al. 1996; Wang et al. 2004; Siersch et al. 2021). The compression along the *c* direction is directly related to the large compression of the MgO_6 octahedral layer described by the oxygen distance between the two opposite faces parallel to the *c*-axis, which has a linear modulus of 309(18) GPa, i.e., more than three times smaller than the linear modulus of the oxygen distance of the SiO_6 octahedral layer (M = 1428(246) GPa) (Figure 7). The compression along the *a*-axis, is likely dominated by the compression of the distance between the oxygens (O···O distance) forming the edges of the shared faces of octahedra that are perpendicular to the *c*-axis, which is much stiffer, with a linear modulus of 848(127) GPa (Figure 7). In the corundum structure, all AlO_6 octahedral layers and face-sharing O···O distances have similar compressibilities (M_{AlO_6} = 639(97) GPa and $M_{O\cdots O}$ = 784(108) GPa, respectively) leading to an isotropic compression of the *a* and *c* axes. With increasing Al content, the compressibility of the MgO_6 and SiO_6 octahedra will approach one another and hence give rise to more isotropic axial compressibility as seen for Ak80 (Figure 5c).

Implications

A bulk elastic property of a mineral in a solid solution, Ψ_{SS}, can be estimated by assuming a linear summation of the individual elastic properties of the corresponding end-members, i.e.:

This is the peer-reviewed, final accepted version for American Mineralogist, published by the Mineralogical Society of America.
The published version is subject to change. Cite as Authors (Year) Title. American Mineralogist, in press.
DOI: https://doi.org/10.2138/am-2022-8257. http://www.minsocam.org/

$$\Psi_{SS} = \frac{1}{\sum_{i=1}^{n} \frac{1}{m_i V_i} \sum_{i=1}^{n} \frac{m_i V_i}{\Psi_i}}$$

where Ψ_i are the elastic properties of component *i*, m_i and V_i are the mole and volume fractions of component *i*, respectively, and *n* is the number of end-members in the solid solution (Chantel 2012). The use of such a relation is problematic, however, in the case of the akimotoite – corundum join. Investigation of the individual unit-cell parameters shows that they behave in a strongly non-ideal fashion and that complete mixing between the two end-members probably does not occur. In fact, changes in unit-cell lattice parameters and octahedral bond lengths imply that the accommodation mechanisms of Al_2O_3 substitution in $MgSiO_3$ akimotoite and of $MgSiO_3$ substitution in corundum are quite different. Most likely related to this is the fact that the akimotoite-corundum join is an example of a system where an elastic property, the bulk modulus in this case, changes in a significantly non-linear fashion across the solid solution. When Al_2O_3 is added to akimotoite the bulk modulus first decreases but must increase again as corundum is approached. This means that the use of the elastic properties of corundum for the calculation of bulk elastic properties, and consequently wave velocities, of Al-bearing akimotoite in mineral physics models, as used in the past (Stixrude and Lithgow-Bertelloni 2005; 2011), will produce values that are inaccurate. To illustrate this problem, the bulk sound velocity, $v_\Phi = \sqrt{K/\rho}$, has been calculated for Ak98 and Ak80 up to 25 GPa using the equation of state parameters determined from measurements made in this study (Figure 8). These are then compared with the bulk sound velocities obtained for the same compositions from a linear interpolation of the elastic properties of akimotoite (Siersch et al. 2021) and corundum (Higo et al. 2018). The bulk sound velocity determined for Ak80 is slower than that of the akimotoite end-member by approximately 0.06 km/s at 20 GPa but the velocity determined through linear mixing of akimotoite and corundum is higher by approximately the same amount, resulting in the linear mixing value over estimating the velocity by approximately 1.3 %.

As the Al_2O_3 content of akimotoite in the mantle probably never reaches values higher than 25 mol% (Kubo and Akaogi 2000), the best way to resolve this discrepancy for linear mixing models is to define a fictive $R\bar{3}$ Al_2O_3 akimotoite end-member. A linear relationship between the bulk modulus of Ak100 and Ak80 gives a value for Ak0 of K_0 = 175 GPa and K_0' = 6.4, which is significantly smaller than the 250 GPa value of corundum (Higo et al. 2018). The effect of this difference, however, when calculating the bulk sound velocity for a harzburgitic composition at adiabatic temperatures at the base of the transition zone will be relatively small because experiments show that under such conditions akimotoite contains only 5 mol% Al_2O_3 and makes up only 15 vol% of the rock (Ishii et al. 2019a). However, experiments at lower temperatures indicate that higher akimotoite Al_2O_3 contents should occur at temperatures compatible with the harzburgitic portion of a subducting slab (Kubo and Akaogi 2000), which would also lead to an increase in the proportion of akimotoite in the rock at the expense of garnet. Further support for this comes from the fact that it was possible to synthesize an akimotoite sample in this study containing 20 mol% Al_2O_3 at 1123 K and 26 GPa. To fully examine the effect of Al_2O_3 in akimotoite on seismic velocities in the transition zone it would be important to also obtain elasticity data, including the shear modulus, at high temperatures and obtain sufficient phase relations data to reliably determine the proportion and composition of akimotoite as a function of pressure and temperature.

Acknowledgements

This study was supported by DFG grants FR1555/11 and KU3447/1. The authors would like to thank Hubert Schulze and Raphael Njul for the preparation of the samples and Leonid Dubrovinsky for his assistance with the Bruker IμS Inside diffractometer. We would like to thank Irene Landi for her help with some aspects of the data collection. We appreciate

461 comments by Masaki Akaogi and Oliver Tschauner that significantly improved the manuscript.
462 Portions of this work were performed at GeoSoilEnviroCARS (The University of Chicago,
463 Sector 13), Advanced Photon Source (APS), Argonne National Laboratory.
464 GeoSoilEnviroCARS is supported by the National Science Foundation – Earth Sciences (EAR
465 – 1634415) and Department of Energy- GeoSciences (DE-FG02-94ER14466). This research
466 used resources of the Advanced Photon Source, a U.S. Department of Energy (DOE) Office of
467 Science User Facility operated for the DOE Office of Science by Argonne National Laboratory
468 under Contract No. DE-AC02-06CH11357.

469

References

Akaogi, M., Tanaka, A., and Ito, E. (2002) Garnet-ilmenite-perovskite transitions in the system $Mg_4Si_4O_{12}$-$Mg_3Al_2Si_3O_{12}$ at high pressures and high temperatures: phase equilibria, calorimetry and implications for mantle structure. Physics of the Earth and Planetary Interiors, 132, 303-324.

Angel, R.J. (2004) Absorption corrections for diamond-anvil pressure cells implemented in the software package Absorb6.0. Journal of Applied Crystallography, 37, 486-492.

Angel, R., Gonzalez-Platas, J., and Alvaro, M. (2014). EosFit7c and a Fortran module (library) for equation of state calculations. Zeitung für Kristallographie, 229(5), 405-419.

Beran, A., and Rossman, G.R. (2006) OH in naturally occurring corundum. European Journal of Mineralogy, 18, 441-447.

Bindi, L., Sirotkina, E.A., Bobrov, A.V., and Irifune, T. (2014) Chromium solubility in $MgSiO_3$ ilmenite at high pressure. Physics and Chemistry of Minerals, 41, 519-526.

Bolfan-Casanova, N., Keppler, H., and Rubie, D.C. (2000) Water partitioning between nominally anhydrous minerals in the MgO-SiO_2-H_2O system up to 24 GPa: implications for the distribution of water in the Earth's mantle. Earth and Planetary Science Letters, 182, 209-221.

Chantel, J. (2012) Measurement of elastic properties of silicates at realistic mantle pressures, 154 p. Ph.D. thesis, University of Bayreuth.

d'Amour, H., Schiferl, D., Denner, W., Schulz, H., and Holzapfel, W.B. (1978) High-pressure single-crystal structure determinations for ruby up to 90 kbar using an automatic diffractometer. Journal of Applied Physics, 49, 4411-4416.

Dewaele, A., Loubeyre, P., and Mezouar, M. (2004) Equations of state of six metals above 94 GPa. Physical Review B, 70, 094112.

493 Dewaele, A., and Torrent, M. (2013) Equations of state of α-Al_2O_3. Physical Review B, 88,
494 064107.

495 Farrugia, L. (1999) *WinGX* suite for small-molecule single-crystal crystallography. Journal of
496 Applied Crystallography, 32, 837-838.

497 Finger, L.W., and Hazen, R.M. (1978) Crystal structure and compression of ruby to 46 kbar.
498 Journal of Applied Physics, 49, 5823-5826.

499 Foley, B.J., and Long, M.D. (2011) Upper and mid-mantle anisotropy beneath the Tonga slab.
500 Geophysical Research Letters, 38, L02303.

501 Gasparik, T. (1990) Phase relations in the transition zone. Journal of Geophysical Research, 95,
502 15,751-15,769.

503 Gonzalez-Platas, J., Alvaro, M., Nestola, F., and Angel, R. (2016) EosFit7-GUI: a new
504 graphical user interface for equation of state calculations, analyses and teaching. Journal of
505 Applied Crystallography, 49, 1377-1382.

506 Higo, Y., Irifune, T., and Funakoshi, K. (2018) Simultaneous high-pressure high-temperature
507 elastic velocity measurement system up to 27 GPa and 1873 K using ultrasonic and synchrotron
508 X-ray techniques. Review of Scientific Instruments, 89, 014501.

509 Horiuchi, H., and Hirano, M. (1982) $MgSiO_3$ (ilmenite-type): single crystal X-ray diffraction
510 study. American Mineralogist, 67, 788-793.

511 Irifune, T., and Ringwood, A.E. (1987) Phase transformations in a harzburgite composition to
512 26 GPa: implications for dynamical behavior of the subducting slab. Earth and Planetary
513 Science Letters, 86, 365-376.

514 Irifune, T., Koizumi, T., and Ando, J. (1996) An experimental study of the garnet-perovskite
515 transformation in the system $MgSiO_3$-$Mg_3Al_2Si_3O_{12}$. Physics of the Earth and Planetary
516 Interiors 96, 147-157.

517 Irifune, T., Higo, Y., Inoue, T., Kono, Y., Ohfuji, H., and Funakoshi, K. (2008) Sound velocities
518 of majorite garnet and the composition of the mantel transition region. Nature, 451, 814-817.

519 Ishii, T., Kojitani, H., and Akaogi, M. (2011) Post-spinel transitions in pyrolite and Mg_2SiO_4
520 and akimotoite-perovskite transition in $MgSiO_3$: Precise comparison by high-pressure high-
521 temperature experiments with multi-sample cell technique. Earth and Planetary Science
522 Letters, 309, 185-197.

523 Ishii, T., Shi, L., Huang, R., Tsujino, N., Druzhbin, D., Myhill, R., Li., Y., Wang, L.,
524 Yamamoto, T., Miyajima, N., Kawazoe, T., Nishiyama, Y., Higo, Y., Tange, Y., and Katsura,
525 T. (2016) Generation of pressures over 40 GPa using Kawai-type multi-anvil press with
526 tungsten carbide anvils. Review of Scientific Instruments, 87(2), 024501.

527 Ishii, T., Kojitani, H., and Akaogi, M. (2019a) Phase Relations of Harzburgite and MORB up
528 to the Uppermost Lower Mantle Conditions: Precise Comparison With Pyrolite by Multisample
529 Cell High-Pressure Experiments With Implication to Dynamics of Subducted Slabs. Journal of
530 Geophysical Research: Solid Earth, 124, 3491–3507.

531 Ishii, T., Liu, Z., and Katsura, T. (2019b) A breakthrough in pressure generation by a Kawai-
532 type multi-anvil apparatus with tungsten carbide anvils. Engineering, 5(3), 434-440.

533 Ito, E., and Yamada, H. (1982) High-pressure research in geophysics, D. Reidel, Dordrecht.
534 Stability Relations of Silicate Spinels, Ilmenites, and Perovskites, pp. 405-419.

535 Kantor, I., Prakapenka, V., Kantor, A., Dera, P., Kurnosov, A., Sinogeikin, S., Dubrovinskaia,
536 N., and Dubrovinsky, L. (2012) BX90: A new diamond anvil cell design for X-ray diffraction
537 and optical measurements. Review of Scientific Instruments, 83(12), 3–8.

Kanzaki, M. (1987) Ultrahigh-pressure relations in the system $Mg_4Si_4O_{12}$-$Mg_3Al_2Si_3O_{12}$. Physics of the Earth and Planetary Interiors, 49, 168-175.

Kato, T., Kinoshita, Y., Nishiyama, N., Wada, K., Zhou, C., and Irifune, T. (2014) Magnesium silicate perovskite coexisting with ringwoodite in harzburgite stagnated at the lowermost mantle transition zone. Physics of the Earth and Planetary Interiors, 232, 26-29.

Kawai, N., Tachimori, M., and Ito, E. (1974) A High Pressure Hexagonal Form of $MgSiO_3$. Proceedings of the Japan Academy, 50, 378-380.

Keppler, H., and Frost, D.J. (2005) Introduction to minerals under extreme conditions. In R. Miletich, Ed. Mineral behaviour at extreme conditions, EMU notes in mineralogy, 7, pp. 1-30. European Mineralogical Union.

Kubo, A., and Akaogi, M. (2000) Post-garnet transitions in the system $Mg_4Si_4O_{12}$-$Mg_3Al_2Si_3O_{12}$ up to 28 GPa: phase relations of garnet, ilmenite and perovskite. Physics of the Earth and Planetary Interiors, 121, 85-102.

Kurnosov, A., Kantor, I., Boffa Ballaran, T., Lindhardt, S., Dubrovinsky, L., Kuznetov, A., and Zehnder, B.H. (2008) A novel gas-loading system for mechanically closing of various types of diamond anvil cells. Review of Scientific Instruments, 79, 045110.

Larson, A.C., and Von Dreele, R.B. (2004) General Structure Analysis System (GSAS), Los Alamos National Laboratory Report LAUR 86-748.

Liu, L.-G. (1977) Ilmenite-type solid solutions between $MgSiO_3$ and Al_2O_3 and some structural systematics among ilmenite compounds. Geochimica et Cosmochimica Acta, 41, 1355-1361.

Liu, Z., Irifune, T., Nishi, M., Tange Y., Arimoto, T., and Shinmei, T. (2016) Phase relations in the system $MgSiO_3$-Al_2O_3 up to 52 GPa and 2000 K. Physics of the Earth and Planetary Interiors, 257, 18-27.

Liu, Z., Nishi, M., Ishii, T., Fei, H., Miyajima, N., Boffa Ballaran, T., Ohfuji, H., Sakai, T., Wang, L., Shcheka, S., Arimoto, T., Tange, Y., Higo, Y., Irifune, T., and Katsura, T. (2017) Phase relations in the system $MgSiO_3$-Al_2O_3 up to 2300 K at lower mantle pressures. Journal of Geophysical Research: Solid Earth, 122, 7775-7788.

McGuire, T.R., Scott, E.J., and Grannis, F.H. (1956) Antiferromagnetism in a Cr_2O_3 Crystal. Physical Review, 102, 1000-1003.

Miyajima, N., El Goresy, A., Dupas-Bruzek, C., Seifert, F., Rubie, D.C., Chen, M., and Xie, X. (2007) Ferric iron in Al-bearing akimotoite coexisting with iron-nickel metal in a shock-melt vein in an L-6 chondrite. American Mineralogist, 92, 1545-1549.

Nowacki, A., Kendall, J.-M., Wookey, J., and Pemberton, A. (2015) Mid-mantle anisotropy in subduction zones and deep water transport. Geochemistry Geophysics Geosystems, 16, 764-784.

Ovsyannikov, S.V., and Dubrovinsky, D.S. (2011) High-pressure high-temperature synthesis of Cr_2O_3 and Ga_2O_3. High Pressure Research, 31, 23-29.

Pamato, M.G., Kurnosov, A., Boffa Ballaran, T., Frost, D.J., Ziberna, L., Giannini, M., Speziale, S., Tkachev, S.N., Zhuralev, K.K., and Prakapenka, V.B. (2016) Single crystal elasticity of majoritic garnets: Stagnant slabs and thermal anomalies at the base of the transition zone. Earth and Planetary Science Letters, 451, 114-124.

Reynard, B., Fiquet, G., Itié, J.-P., and Rubie, D.C. (1996) High-pressure X-ray diffraction study and equation of state of $MgSiO_3$ ilmenite. American Mineralogist, 81, 45-50.

Shannon, R.D. (1976) Revised effective ionic radii and systematic studies of interatomic distances in halides and chalcogenides. Acta Crystallographica, A32, 751-767.

583 Sharp, T.G., Lingemann, C.M., Dupas, C., and Stöffler, D. (1997) Natural occurrence of
584 $MgSiO_3$-ilmenite and evidence for $MgSiO_3$-perovskite in a shocked L chondrite. Science, 277,
585 352-355.

586 Sheldrick, G. (2008) A short history of SHELX. Acta Crystallographica, A64, 112-122.

587 Shiraishi, R., Ohtani, E., Kanagawa, K., Shimojuku, A., and Zhao, D. (2008) Crystallographic
588 preferred orientation of akimotoite and seismic anisotropy of Tonga slab. Nature, 455, 657-660.

589 Siersch, N.C. (2019) The effect of Fe and Al on the elasticity of akimotoite, 203 p. Ph.D. thesis,
590 University of Bayreuth, Bayreuth.

591 Siersch, N.C., Kurnosov, A., Criniti, G., Ishii, T., Boffa Ballaran, T., and Frost, D.J. (2021) The
592 elastic properties and anisotropic behavior of $MgSiO_3$ akimotoite at transition zone pressures.
593 Physics of the Earth and Planetary Interiors, 320, 106786.

594 Stixrude, L., and Lithogow-Bertelloni, C. (2005) Thermodynamics of mantle minerals - I.
595 Physical properties. Geophysical Journal International, 162, 610-632.

596 Stixrude, L., and Lithgow-Bertelloni, C. (2011) Thermodynamics of mantle minerals – II. Phase
597 equilibria. Geophysical Journal International, 184, 1180-1213.

598 Sawamoto, H. (1987) High-Pressure Research in Mineral Physics, American Geophysical
599 Union, Washington, D.C., Phase Diagram of $MgSiO_3$ at Pressures up to 24 GPa and
600 Temperatures up to 2200 °C: Phase Stability and Properties of Tetragonal Garnet., pp. 209-219.

601 Toby, B.H. (2001) EXPGUI, a graphical user interface for GSAS. Journal of Applied
602 Crystallography, 34, 210-213.

603 Tomioka, N., and Fujino, K. (1997) Natural $(Mg,Fe)SiO_3$-Ilmenite and –Perovskite in the
604 Tenham Meteorite. Science, 277, 1084-1086.

605 Vavryčuk, V. (2006) Spatially dependent seismic anisotropy in the Tonga subduction zone: A
606 possible contributor to the complexity of deep earthquakes. Physics of the Earth and Planetary
607 Interiors, 155, 63-72.

608 Wang, Y., Uchida, T., Zhang, J., Rivers, M.L., and Sutton, S.R. (2004) Thermal equation of
609 state of akimotoite $MgSiO_3$ and effects of the akimotoite-garnet transformation on seismic
610 structure near the 660 km discontinuity. Physics of the Earth and Planetary Interiors, 143-144,
611 57-80.

612 Wookey, J. Kendall, J.M., and Barruol, G. (2002) Mid-mantle deformation inferred from
613 seismic anisotropy. Nature, 415, 777-780.

614 Yamanaka, T., Komatsu, Y., Sugahara, M., and Nagai, T. (2005) Structure change of $MgSiO_3$,
615 $MgGeO_3$, and $MgTiO_3$ ilmenites under compression. American Mineralogist, 90, 1301-1307.

616 Zhou, C., Gréaux, S., Nishiyama, N., Irifune, T., and Higo, Y. (2014) Sound velocities
617 measurement on $MgSiO_3$ akimotoite at high pressures and high temperatures with simultaneous
618 in situ X-ray diffraction and ultrasonic study. Physics of the Earth and Planetary Interiors, 228,
619 97-105.

620

621

Figure captions

Figure 1: Evolution of the (a) volume, (b) *a* and (c) *c* unit-cell lattice parameters across the $MgSiO_3$ akimotoite - Al_2O_3 corundum solid solution. The black stars indicate the single-crystals investigated in this study, red and blue circles correspond to the polycrystalline samples, Ak98 and Ak80, respectively. The open black symbols, black circles and green triangles are from the literature. The variation of the unit-cell parameters with Cr_2O_3 content (Bindi et al. 2014) are shown in pink. The dashed pink line connects the akimotoite end-member to the corundum structured Cr_2O_3 end-member (eskolaite, off the diagram) taken from Ovsyannikov and Dubrovinsky (2011).

Figure 2: Octahedral volumes of MgO_6, SiO_6 and AlO_6 as a function of Al_2O_3 content in the akimotoite structure. The MgO_6 and SiO_6 octahedral volumes decrease and increase, respectively, as Al is substituted into the structure. The variation of the octahedral volumes MgO_6 and SiO_6 with Cr_2O_3 content is shown in pink (Bindi et al. 2014). The Cr_2O_3 end-member (eskolaite) octahedral volumes are taken from Ovsyannikov and Dubrovinsky (2011). Dashed lines are linear fits through the octahedral volumes of $MgSiO_3$-bearing corundum/eskolaite and the average octahedral volume of Al(Cr)-bearing akimotoites. The dotted lines show linear fits through the Al/Cr-bearing MgO_6 and SiO_6 octahedral volumes of akimotoite.

Figure 3: Variation with Al_2O_3 and Cr_2O_3 content of the distance between two oxygen atoms belonging to the edges of the face shared between two octahedra. A rapid increase can be observed on the akimotoite and corundum-rich sides similar to the trend observed for the *a*-axis (Figure 1b). The $MgSiO_3$ – Cr_2O_3 solid solution on the other hand (Ovsyannikov and Dubrovinsky 2011; Bindi et al. 2014, pink) shows a linear increase of the O···O distance between the two end-members.

Figure 4: Variation with Al_2O_3 and Cr_2O_3 content of the distance between the oxygen describing the average height of the two face-sharing octahedral layers along the *c*-axis. The

$MgSiO_3$ – Al_2O_3 solid solution is described by a negative non-linear trend whereas the $MgSiO_3$ – Cr_2O_3 system follows linear mixing behavior. These structural features are linked to the behavior of the *c*-axes of both systems reported in Figure 1c.

Figure 5: Variation with pressure of the (a) unit-cell volumes, (b) normalized unit-cell lattice parameters a/a_0 and c/c_0 and (c) c/a ratio for the $MgSiO_3$ akimotoite end-member (single crystal DAC measurements), two Al-bearing akimotoite samples, Ak98 and Ak80 (polycrystalline multi-anvil measurements), and the Al_2O_3 corundum end-member (d'Amour et al. 1978). The solid curves show BM3 EoS fits of the individual data sets measured in this study and Siersch et al. (2021), and BM2 EoS fits of the Al_2O_3 corundum end-member.

Figure 6: Change in volume of the MgO_6 (blue) and SiO_6 (red) octahedra up to 10.83(3) GPa. The solid curves indicate BM2 EoS fits of the individual octahedral volumes. No change in compression mechanism can be observed up to the maximum pressure reached in this study. Akimotoite data (black symbols; Yamanaka et al. 2005) and corundum data (green; d'Amour et al. 1978) are shown for comparison.

Figure 7: Variation with pressure of the distance between the oxygens belonging to the two opposite faces of the same octahedron perpendicular to the *c*-axis: MgO_6 octahedral layer (blue) and SiO_6 octahedral layer (red) as well as the variation of the O···O distance (black) of the edge of the face shared between two octahedra in the akimotoite structure. The solid curves indicate BM2 EoS fits of the individual distances. For comparison, the same distances for the AlO_6 octahedra (green circles and green squares, respectively; d'Amour et al. 1978) are shown.

Figure 8: Bulk sound velocity, v_Φ, of Ak100, Ak98 and Ak80 calculated up to 25 GPa using the equation of state parameters reported in this study. The velocities for the $MgSiO_3$ end-member akimotoite are calculated according to the EoS parameters reported by Siersch et al. (2021), whereas the velocities for corundum are calculated using the EoS parameters reported

671 by Higo et al. (2018). The dashed lines show calculations of v_Φ assuming linear mixing relations

672 between the end member properties of $MgSiO_3$ akimotoite and Al_2O_3 corundum.

673

674

675

This is the peer-reviewed, final accepted version for American Mineralogist, published by the Mineralogical Society of America.
The published version is subject to change. Cite as Authors (Year) Title. American Mineralogist, in press.
DOI: https://doi.org/10.2138/am-2022-8257. http://www.minsocam.org/

676 # Tables

677 ***Table 1:*** *Multi-anvil synthesis conditions, resulting run products and compositions of the akimotoite samples investigated in this study.*

experiment		starting material	pressure (GPa)	temperature (K)	heating (h)	run products	composition	crystal size (μm)
S6925	Ak100	$Mg_{1.15}SiO_{3.15}$ + ~15% H_2O	22	1873[a]	4	akimotoite + melt	$Mg_{0.993(1)}Si_{1.003(1)}O_3$	<500
S7179	Ak99	Ak90Cor10 + ~10% H_2O	22	1773	23	Al_2O_3-rich akimotoite + garnet (+ stishovite)	$Mg_{0.975(8)}Al_{0.016(3)}Si_{1.001(4)}O_3$	<30
I796*	Cor75	Ak40Cor60 + $MgCl_2$	27	2300[a]	3.3	$MgSiO_3$-rich corundum + MgO + melt	$Al_{1.501(9)}Mg_{0.239(5)}Si_{0.260(6)}O_3$	<100
I789*	Cor80	Ak40Cor60 + $MgCl_2$	27	2100[a]	2	$MgSiO_3$-rich corundum + MgO + melt	$Al_{1.599(11)}Mg_{0.192(8)}Si_{0.209(4)}O_3$	<100
S7237a*	Cor81	Ak40Cor60 + $MgCl_2$	24	1673[a]	2	$MgSiO_3$-rich corundum + MgO + melt	$Al_{1.628(12)}Mg_{0.162(4)}Si_{0.186(5)}O_3$	<250
S7156b	Cor92	Ak20Cor80 + ~10% $Al(OH)_3$	24	1873	22	$MgSiO_3$-rich corundum + hydrous Al-phases + melt	$Al_{1.847(4)}Mg_{0.073(3)}Si_{0.080(2)}O_3$	<250
S7156a	Cor97	Ak10Cor90 + ~10% $Al(OH)_3$	24	1873	22	$MgSiO_3$-rich corundum + hydrous Al-phases + melt	$Al_{1.947(3)}Mg_{0.025(2)}Si_{0.028(2)}O_3$	<200
S7203	Cor100	Al_2O_3:$Al(OH)_3$ (6:4)	24	1873	25.5	corundum + hydrous Al phases + melt	$Al_{1.962(2)}O_3$	<250
S6741	Ak98	Ak2Cor98 glass	27	1173	1	akimotoite	$Mg_{0.983(7)}Al_{0.041(10)}Si_{0.977(7)}O_3$	<3
I444	Ak80	Ak20Cor80 glass	26	1123	1	akimotoite	$Mg_{0.820(7)}Al_{0.405(7)}Si_{0.775(11)}O_3$	<5

678 [a] temperature estimated from power-temperature relationships, Ak: akimotoite, Cor: corundum.
679 * Synthesis with $MgCl_2$ as flux
680

681

This is the peer-reviewed, final accepted version for American Mineralogist, published by the Mineralogical Society of America.
The published version is subject to change. Cite as Authors (Year) Title. American Mineralogist, in press.
DOI: https://doi.org/10.2138/am-2022-8257. http://www.minsocam.org/

682 ***Table 2:*** *Unit-cell lattice parameters of single-crystals belonging to the akimotoite-corundum*

683 *system determined in this study.*

experiment		Al_2O_3 (mol)	*a* (Å)	*c* (Å)	*V* (Å^3)
S6925	Ak100	0.000	4.7288(1)	13.5609(4)	262.62(1)
S7179	Ak99	0.008	4.7293(1)	13.5503(1)	262.47(1)
I796	Cor75	0.751	4.7703(3)	13.0189(4)	256.56(3)
I789	Cor80	0.800	4.7678(1)	13.0172(2)	256.27(2)
S7237a	Cor81	0.814	4.7599(2)	13.0113(5)	255.29(2)
S7156a	Cor92	0.924	4.7624(2)	12.9996(4)	255.34(3)
S7156b	Cor97	0.974	4.7603(15)	12.9969(30)	255.06(17)
S7203	Cor100	1.000	4.7594(6)	12.9903(8)	254.83(7)

684

685

686

687

688

689

690

691

692

693

694

Table 3: *Unit-cell lattice parameters of the $MgSiO_3$ akimotoite end-member and two Al-bearing akimotoite samples; Ak98 and Ak80, measured at different pressures. For Ak100, the pressure has been determined using the ruby fluorescence calibration by Dewaele et al. (2004). For Ak98 and Ak80, pressure was calculated from simultaneously measuring the density and sound wave velocities of the samples in combined X-ray diffraction and ultrasonic measurements (Siersch 2019).*

P (GPa)	*a* (Å)	*c* (Å)	*V* (Å^3)
Ak100			
0.0001(1)[a]	4.7282(1)	13.5587(1)	262.51(2)
0.87(3)	4.7231(2)	13.5354(1)	261.49(2)
2.12(11)[a]	4.7152(4)	13.5013(3)	259.96(4)
3.39(3)	4.7077(2)	13.4681(2)	258.50(3)
8.07(11)[a]	4.6805(3)	13.3500(2)	253.28(3)
9.15(1)	4.6742(4)	13.3240(3)	252.10(5)
8.10(20)	4.6804(9)	13.3482(7)	253.23(10)
10.57(20)[a]	4.6671(9)	13.2906(6)	250.71(10)
Ak98			
0.0001	4.7302(3)	13.545(2)	262.47(2)
4.65	4.7008(6)	13.427(2)	256.95(4)
9.63	4.6724(3)	13.309(2)	251.62(3)
13.22	4.6528(4)	13.235(2)	248.13(3)
14.60	4.6451(5)	13.211(2)	246.86(4)
16.90	4.6350(3)	13.158(2)	244.81(2)
19.22	4.6232(5)	13.119(2)	242.84(3)
20.56	4.6166(5)	13.097(1)	241.74(3)

23.27	4.6029(5)	13.058(2)	239.59(3)
24.86	4.5938(6)	13.043(2)	238.37(3)
20.06	4.6182(5)	13.110(2)	242.15(3)
21.85	4.6093(5)	13.082(2)	240.70(3)
21.93	4.6082(5)	13.085(2)	240.64(4)
23.60	4.5988(6)	13.067(2)	239.33(3)
19.76	4.6199(6)	13.114(2)	242.40(3)
Ak98			
0.0001	4.7297(3)	13.542(1)	262.34(2)
11.12	4.6681(8)	13.254(2)	250.13(6)
7.73	4.6824(7)	13.355(3)	253.58(6)
18.51	4.6287(13)	13.120(3)	243.43(6)
16.17	4.6402(22)	13.163(6)	245.45(10)
23.46	4.5996(9)	13.068(3)	239.44(6)
20.88	4.6159(12)	13.087(3)	241.48(7)
22.07	4.6067(11)	13.088(3)	240.53(6)
20.88	4.6128(10)	13.105(3)	241.48(5)
Ak80			
0.0001	4.7526(4)	13.349(2)	261.12(3)
11.04	4.6771(5)	13.128(2)	248.70(3)
7.62	4.6972(5)	13.199(2)	252.21(3)
11.42	4.6766(5)	13.111(2)	248.33(3)
12.90	4.6690(5)	13.079(2)	246.91(3)
15.38	4.6541(6)	13.041(2)	244.62(3)
16.25	4.6514(5)	13.015(2)	243.85(3)

19.56	4.6311(7)	12.977(3)	241.02(4)
22.71	4.6146(7)	12.931(3)	238.48(4)
24.51	4.6119(8)	12.872(4)	237.10(5)

[a] Full intensity data was collected at these pressure points.

This is the peer-reviewed, final accepted version for American Mineralogist, published by the Mineralogical Society of America.
The published version is subject to change. Cite as Authors (Year) Title. American Mineralogist, in press.
DOI: https://doi.org/10.2138/am-2022-8257. http://www.minsocam.org/

Figures

Figure 1a

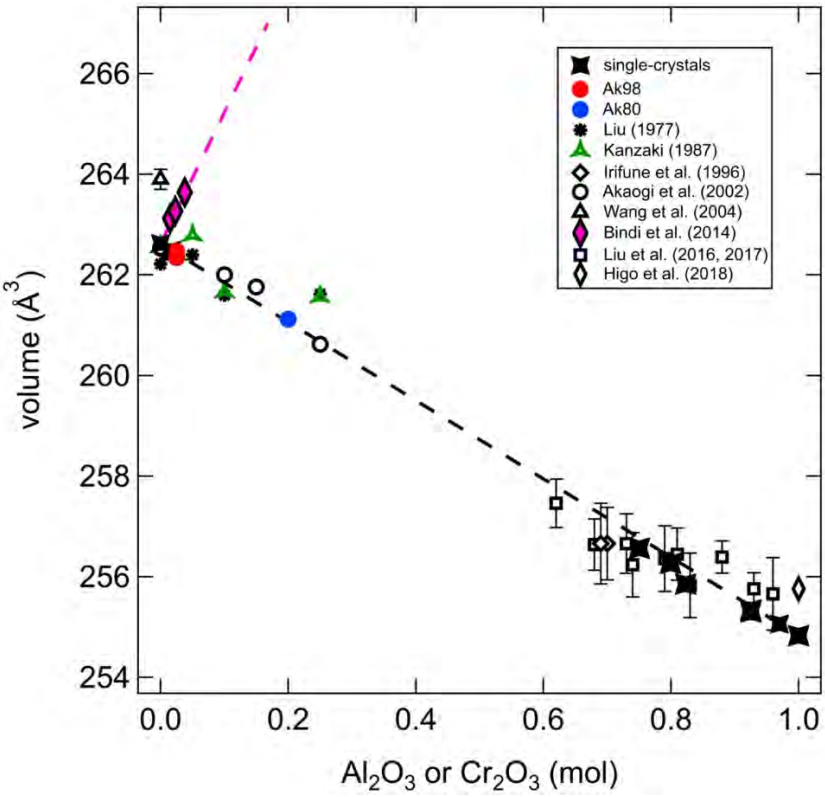

Figure 1b

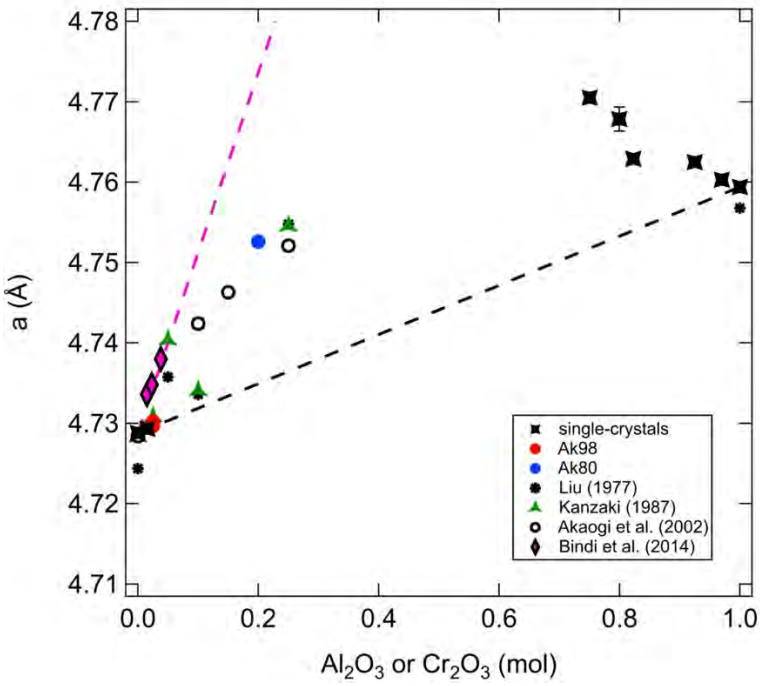

This is the peer-reviewed, final accepted version for American Mineralogist, published by the Mineralogical Society of America.
The published version is subject to change. Cite as Authors (Year) Title. American Mineralogist, in press.
DOI: https://doi.org/10.2138/am-2022-8257. http://www.minsocam.org/

707 **Figure 1c**

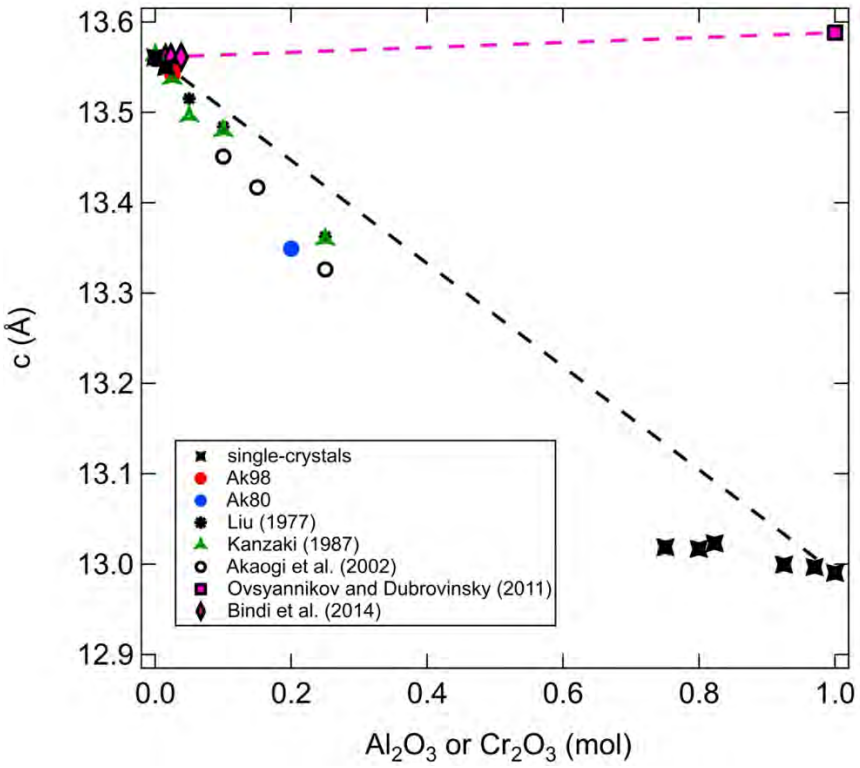

708

709

710

711

712

713

714

715

716

717

718

719 **Figure 2**

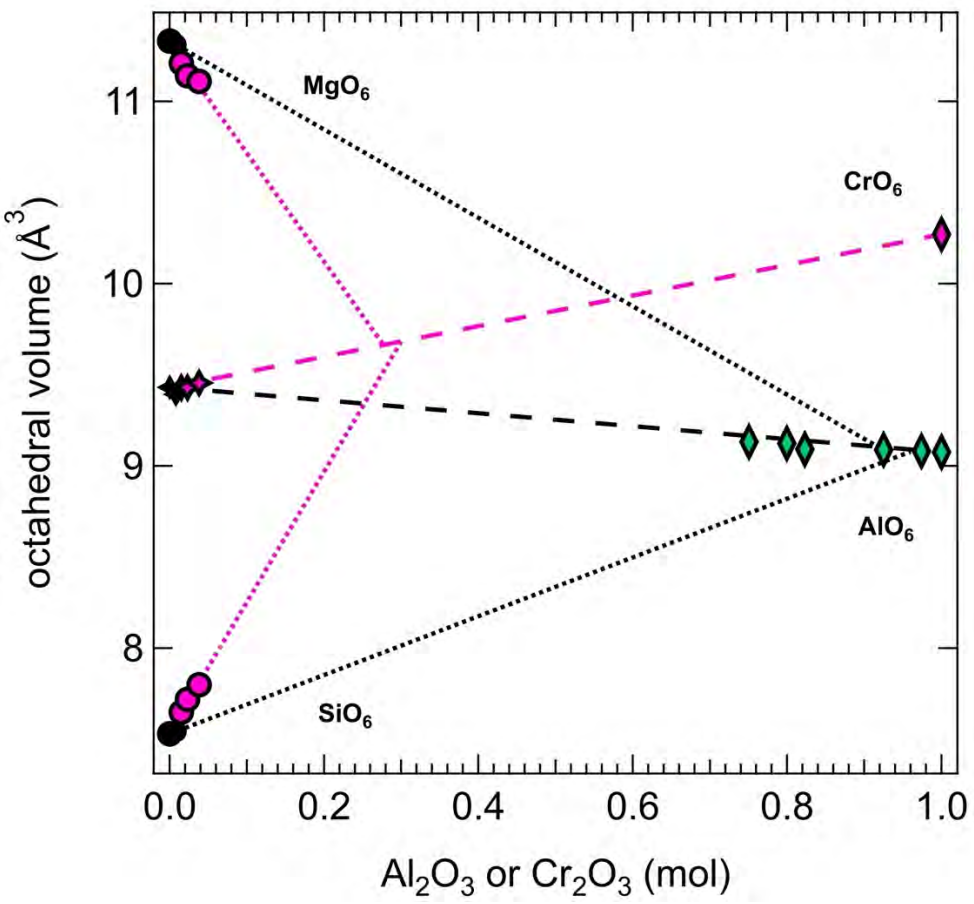

720

721

722

723

724

725

726

727

728

729

730 **Figure 3**

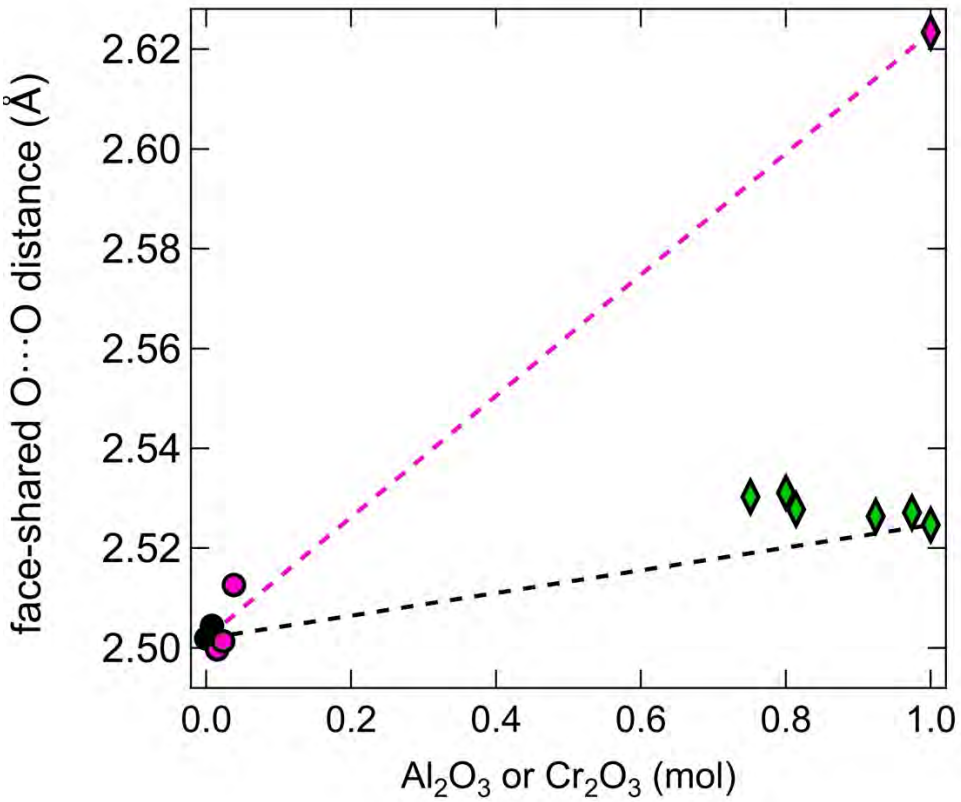

731

732

733

734

735

736

737

738

739

740

741

This is the peer-reviewed, final accepted version for American Mineralogist, published by the Mineralogical Society of America.
The published version is subject to change. Cite as Authors (Year) Title. American Mineralogist, in press.
DOI: https://doi.org/10.2138/am-2022-8257. http://www.minsocam.org/

742 **Figure 4**

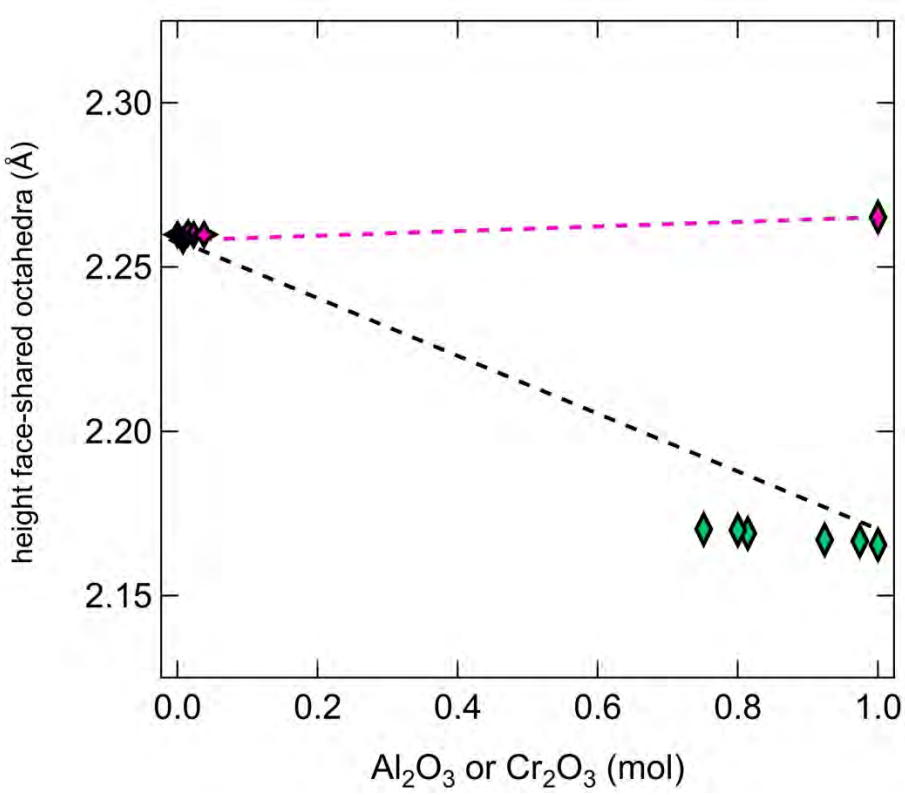

743

744

745

746

747

748

749

750

751

752

753

This is the peer-reviewed, final accepted version for American Mineralogist, published by the Mineralogical Society of America.
The published version is subject to change. Cite as Authors (Year) Title. American Mineralogist, in press.
DOI: https://doi.org/10.2138/am-2022-8257. http://www.minsocam.org/

754 **Figure 5a**

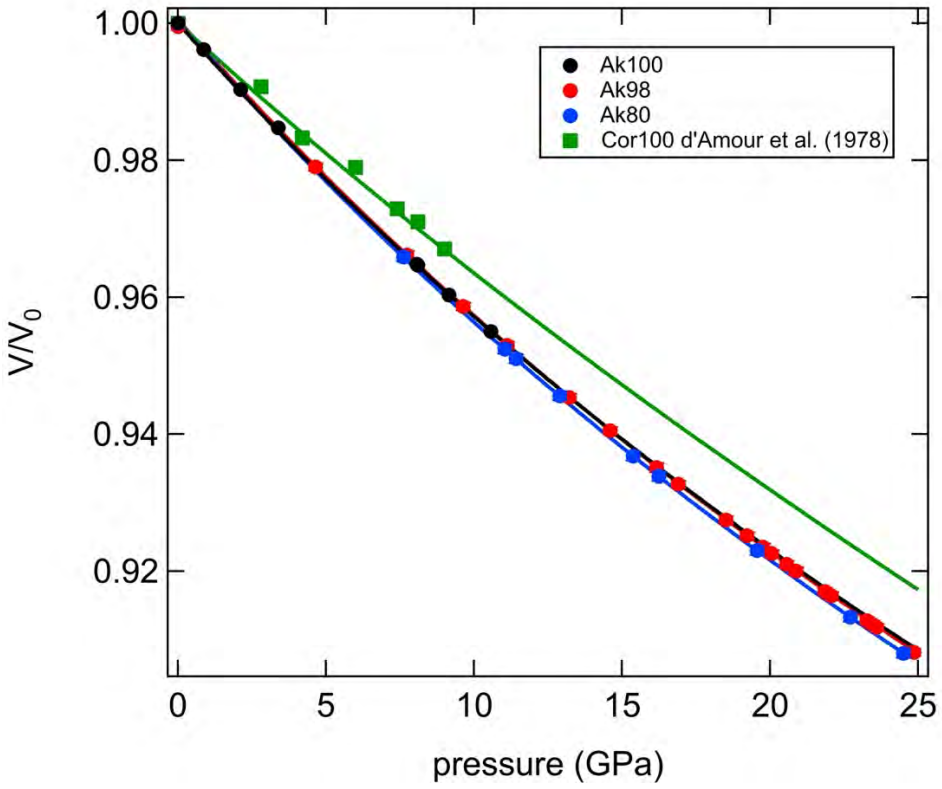

755

756 **Figure 5b**

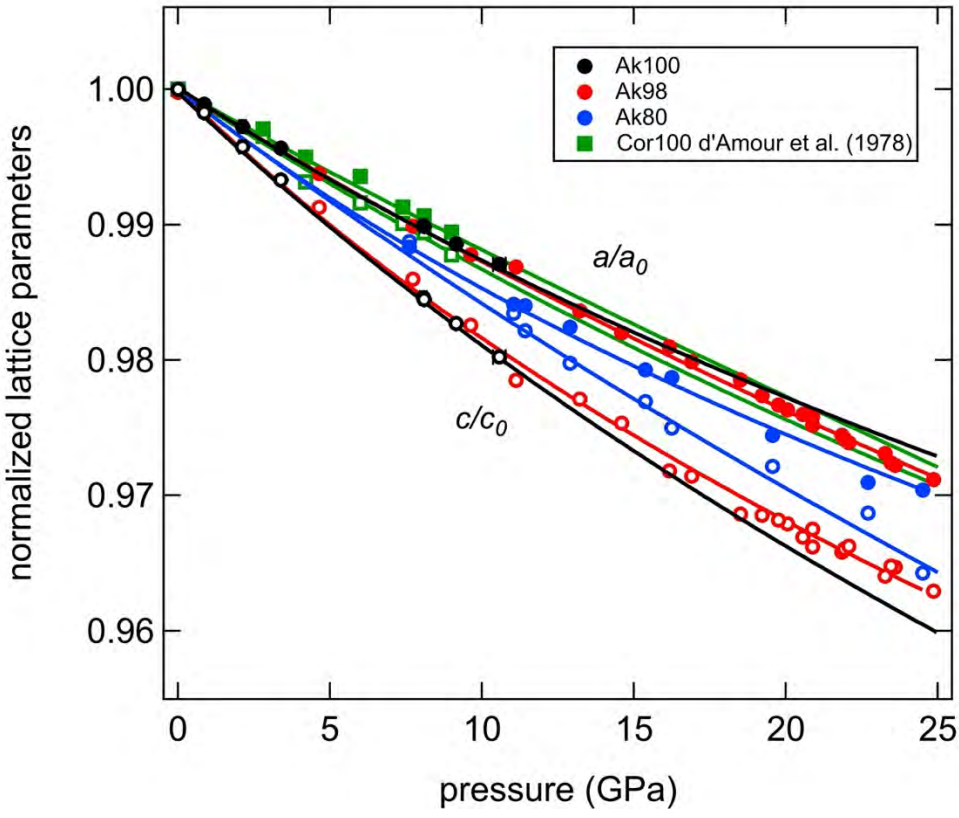

757

This is the peer-reviewed, final accepted version for American Mineralogist, published by the Mineralogical Society of America.
The published version is subject to change. Cite as Authors (Year) Title. American Mineralogist, in press.
DOI: https://doi.org/10.2138/am-2022-8257. http://www.minsocam.org/

758 **Figure 5c**

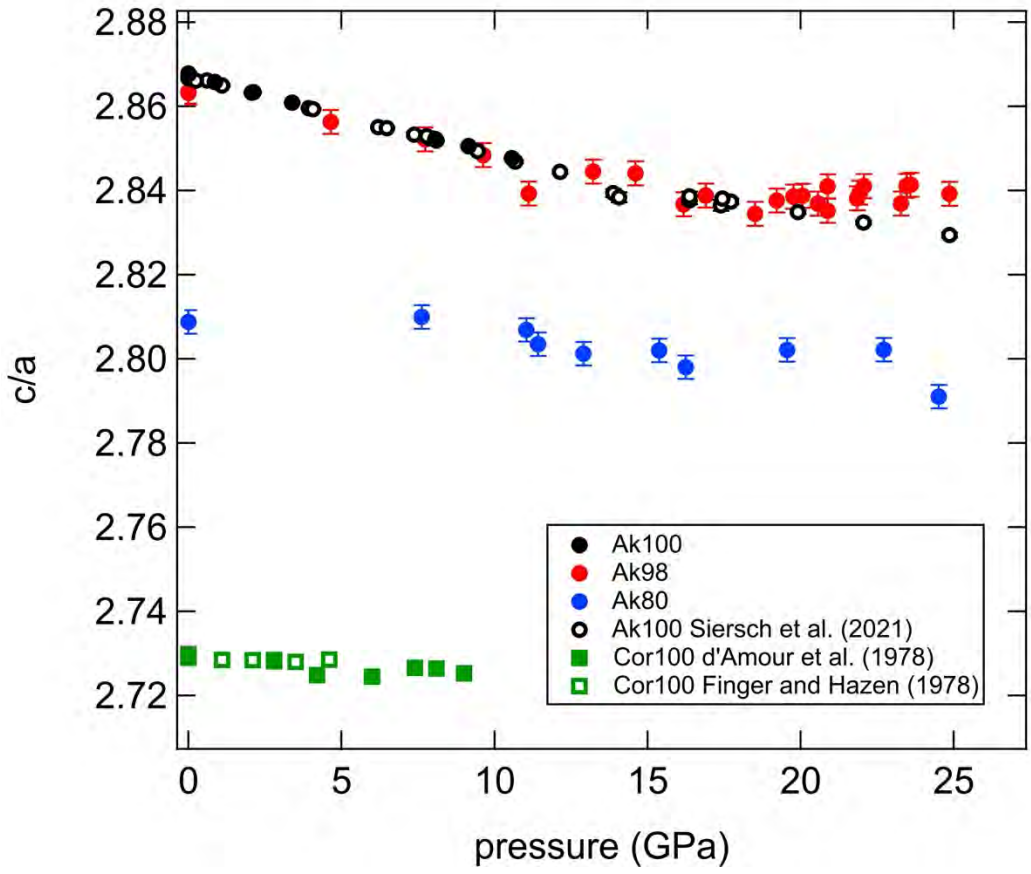

759

760

761

762

763

764

765

766

767

768

This is the peer-reviewed, final accepted version for American Mineralogist, published by the Mineralogical Society of America.
The published version is subject to change. Cite as Authors (Year) Title. American Mineralogist, in press.
DOI: https://doi.org/10.2138/am-2022-8257. http://www.minsocam.org/

769 **Figure 6**

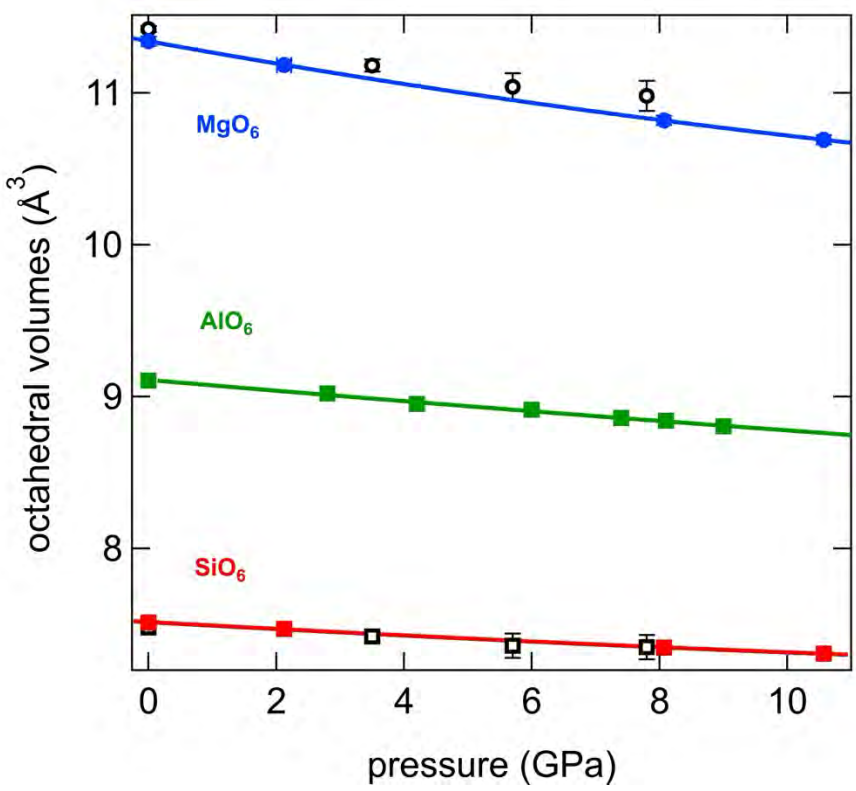

770

771

772

773

774

775

776

777

778

779

780

This is the peer-reviewed, final accepted version for American Mineralogist, published by the Mineralogical Society of America.
The published version is subject to change. Cite as Authors (Year) Title. American Mineralogist, in press.
DOI: https://doi.org/10.2138/am-2022-8257. http://www.minsocam.org/

781 **Figure 7**

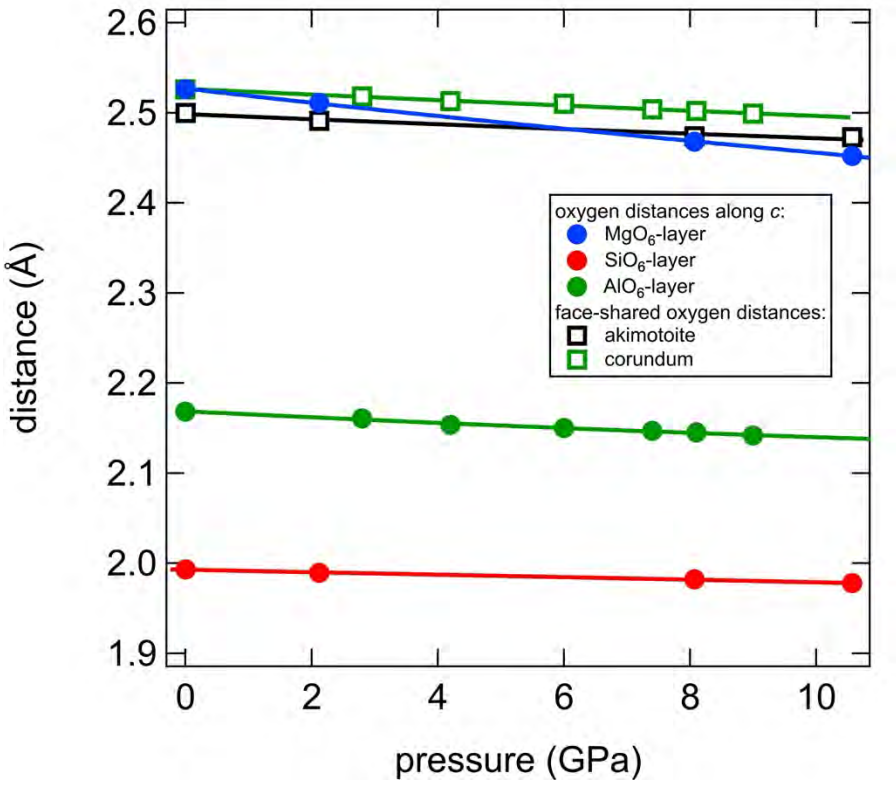

782

783

784

785

786

787

788

789

790

791

792

This is the peer-reviewed, final accepted version for American Mineralogist, published by the Mineralogical Society of America.
The published version is subject to change. Cite as Authors (Year) Title. American Mineralogist, in press.
DOI: https://doi.org/10.2138/am-2022-8257. http://www.minsocam.org/

793 **Figure 8**

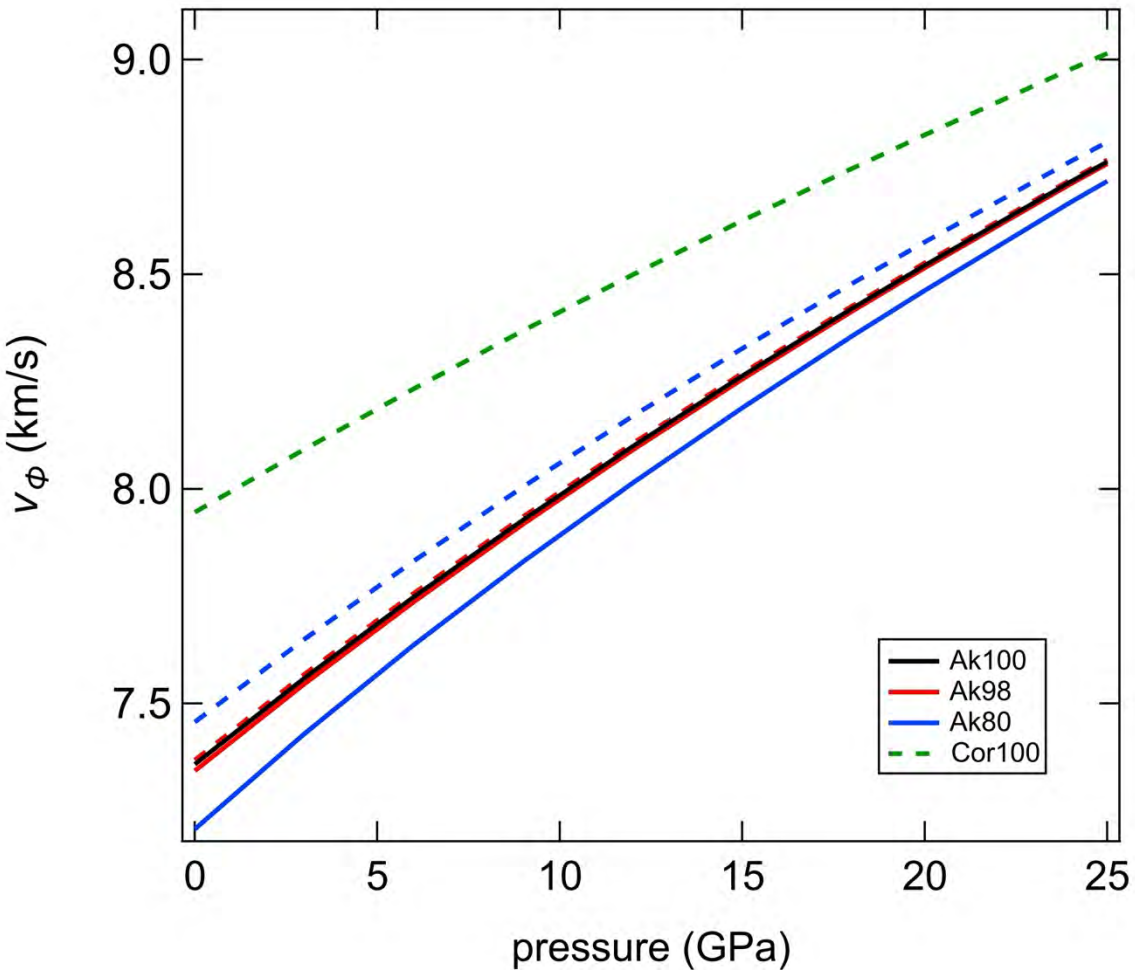

794

795

796

797

798

799

800

801

802